Delft University of Technology

Air-stable, aluminium oxide encapsulated graphene phototransistors

Rojas Castiglione, Tomás ; Pucher, Thomas ; Dockx, K.; Contreras, Guillermo Aburto; Sanz Biava, Diego ; Briceno Elchiver, Benjamín ; Buscema, M.; Castellanos-Gomez, Andres; van der Zant, H.S.J.; Dulic, Diana

DOI
10.1088/1361-6528/ad9df0

Publication date
2025

Document Version
Final published version

Published in
Nanotechnology

Citation (APA)
Rojas Castiglione, T., Pucher, T., Dockx, K., Contreras, G. A., Sanz Biava, D., Briceno Elchiver, B., Buscema, M., Castellanos-Gomez, A., van der Zant, H. S. J., & Dulic, D. (2025). Air-stable, aluminium oxide encapsulated graphene phototransistors. *Nanotechnology*, *36*(9), Article 095706. https://doi.org/10.1088/1361-6528/ad9df0

Important note
To cite this publication, please use the final published version (if applicable). Please check the document version above.

Copyright
Other than for strictly personal use, it is not permitted to download, forward or distribute the text or part of it, without the consent of the author(s) and/or copyright holder(s), unless the work is under an open content license such as Creative Commons.

Takedown policy
Please contact us and provide details if you believe this document breaches copyrights. We will remove access to the work immediately and investigate your claim.

This work is downloaded from Delft University of Technology.
For technical reasons the number of authors shown on this cover page is limited to a maximum of 10.

PAPER • OPEN ACCESS

Air-stable, aluminium oxide encapsulated graphene phototransistors

To cite this article: Tomás Rojas Castiglione *et al* 2025 *Nanotechnology* **36** 095706

View the article online for updates and enhancements.

You may also like

- High-responsivity turbostratic stacked graphene photodetectors using enhanced photogating
Masaaki Shimatani, Naoki Yamada, Shoichiro Fukushima et al.

- Highly sensitive visible to infrared $MoTe_2$ photodetectors enhanced by the photogating effect
Hai Huang, Jianlu Wang, Weida Hu et al.

- Modeling of graphene photodetector based on photogating effect for circuits simulation
Haozhou Li, Zeyuan Shi, Longcheng Que et al.

UNITED THROUGH SCIENCE & TECHNOLOGY
ECS The Electrochemical Society
Advancing solid state & electrochemical science & technology
248th
ECS Meeting
Chicago, IL
October 12-16, 2025
Hilton Chicago
Science +
Technology +
YOU!
SUBMIT
ABSTRACTS by
March 28, 2025
SUBMIT NOW

This content was downloaded from IP address 145.90.37.70 on 31/12/2024 at 07:32

OPEN ACCESS
IOP Publishing

Nanotechnology

Nanotechnology **36** (2025) 095706 (9pp)

https://doi.org/10.1088/1361-6528/ad9df0

Air-stable, aluminium oxide encapsulated graphene phototransistors

Tomás Rojas Castiglione[1,2], Thomas Pucher[3], Kaj Dockx[4,5], Guillermo Aburto Contreras[2], Diego Sanz Biava[2], Benjamín Briceño Elchiver[1,6], Michele Buscema[4], Andres Castellanos-Gomez[3], Herre van der Zant[5] and Diana Dulić[1,2,*]

[1] Department of Physics (FCFM), Universidad de Chile, Santiago, Chile
[2] Department of Electrical Engineering (FCFM), Universidad de Chile, Santiago, Chile
[3] 2D Foundry Research Group, Instituto de Ciencia de Materiales de Madrid (ICMM-CSIC), Madrid, Spain
[4] Applied Nanolayers B.V., Zoetermeer, The Netherlands
[5] Kavli Institute of Nanoscience, Delft University of Technology, Delft, The Netherlands
[6] Institute of Physics, University of Augsburg, Augsburg, Germany

E-mail: ddulic@ing.uchile.cl

Received 25 October 2024, revised 4 December 2024
Accepted for publication 12 December 2024
Published 30 December 2024

Abstract

Graphene has garnered significant interest in optoelectronics due to its unique properties, including broad wavelength absorption and high mobility. However, its weak stability in ambient conditions requires encapsulation for practical applications. In this study, we investigate graphene CVD-grown field-effect transistors fabricated on Si/SiO_2 wafers, encapsulated with aluminum oxide (Al_2O_3) of different thicknesses. We measure and analyze their optoelectronic response across wavelengths from near-ultraviolet to near-infrared. We find that, while having a negligible role in the photogating process, the Al_2O_3 layer leads to stable and reproducible transferring curves operating in ambient conditions for over a month, with stable responsivities up to 1.5 A W^{-1} at the shortest wavelength. Moreover, the transferring curves are stable at elevated temperatures up to 107 °C. We also show that the sample performance can be tuned by changing the thickness of the SiO_2 and Al_2O_3 layer which brings further perspectives in developing robust sample technologies, especially in the ultraviolet region where the responsivity increases. Aluminum oxide encapsulated graphene-based photodetectors can thus be interesting for applications in air and at elevated temperatures.

Supplementary material for this article is available online

Keywords: stable, aluminium oxide, passivated, graphene, phototransistors, photogating, ambient condition detector

* Author to whom any correspondence should be addressed.

Original Content from this work may be used under the terms of the Creative Commons Attribution 4.0 licence. Any further distribution of this work must maintain attribution to the author(s) and the title of the work, journal citation and DOI.

© 2024 The Author(s). Published by IOP Publishing Ltd

1. Introduction

Since its discovery, graphene has attracted interest in optoelectronics [1, 2] and photodetection due to its ability to absorb light over a broad wavelength range and fast response times [3, 4]. However, graphene has a low absolute value of light absorption (2.3 %) when compared to bulk materials used in photodetectors [4, 5], which limits the sensitivity of photodetectors made of it. Therefore, a wide variety of hybrid structures combining graphene with other semiconductors, geometries and detection schemes have been investigated and demonstrated to have significant improvements in their performance [6–9]. In parallel, practical challenges have been addressed to take research beyond the proof-of-principle stage [10, 11]. The first obstacle herein is the stability of graphene in an ambient environment over long periods of time, which has been partially solved by implementing schemes for encapsulation of the graphene surface [12, 13].

Another obstacle has been large-scale production. While being compatible with CMOS technology, most of the initial reports focused on individual or a small number of samples, typically fabricated using the mechanical exfoliation method [5, 14–17]. Advances in chemical vapor deposition (CVD) growing techniques now allow the growth of high-quality graphene across a large area which opens routes toward commercial applications [11, 18]. This study advances beyond conventional photodetector investigations by demonstrating the stability and reproducibility of Al_2O_3-encapsulated graphene devices under both ambient and elevated temperature conditions. These findings are particularly relevant for applications in harsh environments, such as those encountered in space missions. For instance, low Earth orbit satellites, including CubeSats, can experience external temperatures reaching up to 60 °C [19], hence usually tests with temperatures up to 70 °C or 80 °C before launches are carried out.

Due to its compatibility with CMOS technology, CVD-grown graphene with aluminum oxide (Al_2O_3) encapsulation, deposited via atomic layer deposition (ALD), has been studied for various ambient condition applications. These include solar cells [20], DNA and DNA-protein complex detectors [21], encapsulation of organic light-emitting diodes for flexible screens [22], graphene gas barriers [23], and graphene field-effect transistors (gFETs) [24–26]. Notably, gFETs encapsulated in this manner demonstrate stable transfer curves for up to two months [25]. In addition to these applications, CVD-grown graphene, in conjunction with ALD of aluminum oxide (Al_2O_3), has been utilized in graphene-based photodetectors designed to operate under ambient conditions [27–32]. However, reports on such devices often feature only a single sample [30, 31], and typically, only a limited number of wavelengths with varying power are tested. Additionally, there is a notable lack of studies on the stability of the photoresponse, highlighting an area for further exploration.

This study explores the impact of Al_2O_3 encapsulation on the stability of gFETs fabricated on Si/SiO_2 wafers for applications in light detection. The goal is to develop robust and reproducible samples operating in both, ambient conditions over long periods of time and harsh surroundings (e.g. at elevated temperatures). We investigate the effect of Al_2O_3 encapsulation on the optoelectronic performance, focusing on photocurrent, responsivity, power dependence, and the speed of radiation response across a wide spectrum of wavelengths, from near-ultraviolet (NUV) to near-infrared (NIR). Additionally, we monitor the stability of the samples over time and after variations in temperature in the range from room temperature to 107 °C. To understand if the Al_2O_3 encapsulation has any effect on the response of the samples to light, we studied samples with different Al_2O_3 thicknesses, as well as, bare graphene samples. For these last ones, we also tested different SiO_2 thicknesses.

2. Samples

For the fabrication of the gFETs, a contact-first integration scheme is adopted with the p-doped Si substrate acting as a global back gate (figure 2). Graphene is grown in a home-built CVD reactor and dry transferred onto the target wafer; both processes are proprietary to Applied Nanolayers (ANL). The gold source and drain electrodes with a Ti sticking layer underneath are pre-patterned on the SiO_2/Si wafer before the graphene is transferred onto them. Then, the graphene is patterned into channels using reactive ion etching in oxygen, and finally the aluminum oxide layer is deposited by ALD. The ALD encapsulating Al_2O_3 is removed from the contact region by wet Tetramethylammonium Hydroxide (TMAH) etching. The samples have been produced in the same batch as earlier work [33], which describes the fabrication in more detail.

Each wafer contains 240 chips, each with 10 gFETs that come in five different aspect ratios as seen in figure 1. For the detailed dimensions, see table 1. For this study, we concentrate on 9 samples; their characteristics are described in table 2. Samples with different thicknesses Al_2O_3 are created using samples with a 40 nm layer and reducing the thickness by wet TMAH etching. For sample 6, the whole ALD Al_2O_3 layer has been removed in this way. Sample 7 is a reference sample from a different wafer. It comprises just of the transferred CVD on the SiO_2/Si wafer; however, the SiO_2 oxide layer is about three times thinner in this case.

3. Methodology

The experimental setup consists of a constant voltage source applied across the graphene channel, with an ammeter measuring the resulting current. A variable voltage source is connected to the gate, allowing for adjustable gate voltages. Finally, an optical circuit can be coupled to the sample via an optical tube and fiber optics. The described circuit can be seen in figure 2. Access to contacts is facilitated by gold-coated needles mounted on micromanipulators, which directly connect the gold pads. To access the gate from the top, a scratch is made in the substrate far away from the gFETs. All

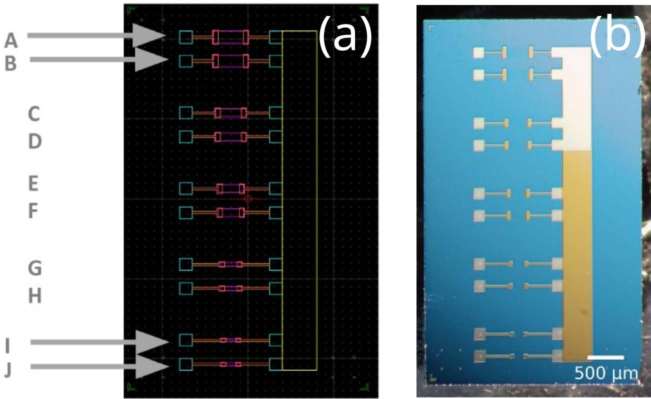

Figure 1. (a) CAD design and (b) picture of one chip with 10 gFETs.

Table 1. Dimensions of the samples in one chip.

Device	Length (μm)	Width (μm)
A, B	300	150
C, D	250	100
E, F	200	100
G, H	150	50
I, J	120	30

Table 2. Specifications of all samples used in the study. The absence of Al_2O_3 is represented by a dash (-).

Sample	SiO_2 (nm)	Al_2O_3 (nm)	Length (μm)	Width (μm)	Etched Al_2O_3
1	285	40	200	100	No
2	285	40	200	100	No
3	285	21	200	100	Yes
4	285	17	200	100	Yes
5	285	40	200	100	No
6	285	—	200	100	Yes
7	90	—	200	100	No
8	285	40	300	150	No
9	285	40	200	100	No

experiments are performed in an ambient environment in a homemade set-up. More details about the measurement procedure can be found in the SI.

Samples are illuminated using THORLABS Fiber-Coupled LEDs emitting light at various wavelengths ranging from 365 to 850 nm [34].The Full Width at Half Maximum (FWHM) for the LED's spectrum ranges from approximately 10 to around 30 nm, except for the LED emitting light at 505 nm, which has an FWHM of 105 nm. The illumination is directed through an eyepiece focused on the sample. The spot size is about 105783 μm^2 and thus covers the entire device. A Python script regulates the power of the LEDs, with power calibration performed by sweeping a voltage source attached to the LED's driver and measuring the corresponding power using a THORLABS PM100D with a S120VC sensor attached.

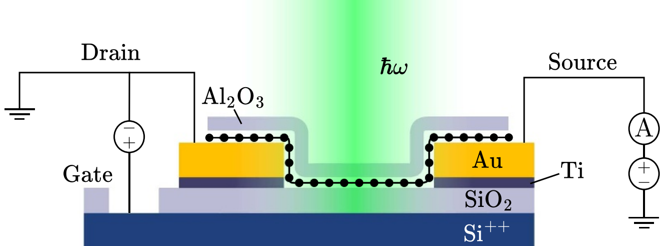

Figure 2. Side view of an ALD encapsulated graphene field-effect sample with a doped silicon back gate. The gold pads serve as source and drain terminals, exposed by TMAH etching. The back gate is contacted by scratching the SiO_2 with a diamond tip pencil, indicated by the discontinuity in the SiO_2 layer. Voltage is applied between the drain and source, with current monitored through the channel. The gate voltage is varied by an additional supply and a voltage-controlled LED is optically coupled to the setup for time-dependent measurements. Thicknesses of Au, and Ti are 55 nm and 5 nm, respectively.

For the data acquisition, we first measure transfer curves (source-drain current, I_{SD}, vs. gate voltage, V_G) under dark conditions and illumination, as shown in figure 3. The gate voltage is swept from −35 to 35 V, and a constant source-drain voltage of 75 mV is applied throughout all experiments. During the illumination, the sample is exposed to light for approximately 3 minutes. For the temperature-dependent measurements, the samples are placed on a MHP30 hot plate, and data is collected after the temperature had stabilized.

The time-dependent current is also measured while modulating the light intensity, as shown in figure 5. This is done at three gate voltages: −15, −4, and 4 V, relative to the Charge Neutrality Point (CNP). Once the gate voltage is set to the desired value, an illumination sequence of OFF-ON-OFF is performed, with each phase lasting 60 s. Here, we focus on the ON-OFF part of the sequence, reporting 60 s of illumination followed by 60 s of darkness. This ensures that transients unrelated to photodetection, such as capacitive coupling, are excluded. Examples of additional data can be found in figures S5, S7, and S6 in the supplementary information (SI).

In order to quantify the response of the samples, an important quantity is the photocurrent I_{ph}, defined as the change in current due to illumination. From the measurements, we calculate the responsivity ($\mathcal{R}$), defined as the photocurrent per unit of incident power (P):

$$\mathcal{R} = \frac{I_{ph}}{P} \propto I_{ph}, \tag{1}$$

where P is determined by measuring the light spot power and scaling it by the sample-to-spot area ratio, approximately 0.19.

To evaluate the temporal response of the samples, we use the 10%–90% rise (or fall) time. This is defined as the time it takes for a signal to shift from 10% to 90% of its highest or lowest value after the illumination is applied (or removed).

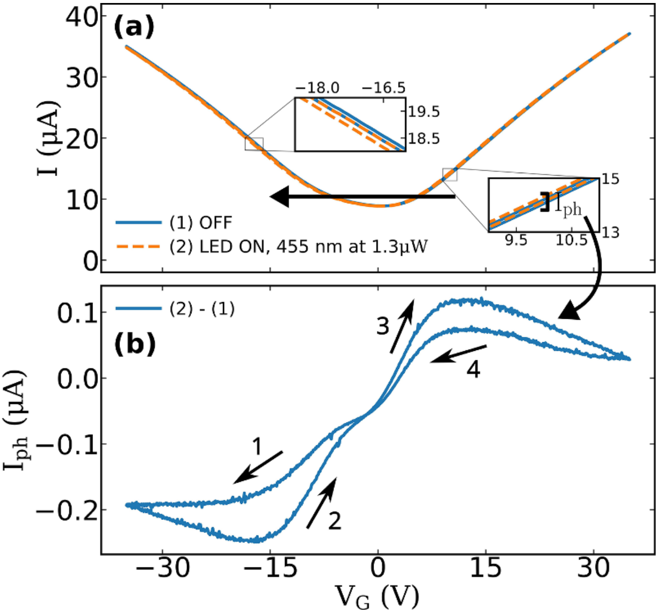

Figure 3. (a) Transfer curves (forward and reverse sweeps) for Sample 2 in the dark (blue curve) and under 455 nm light illumination at 1.3 μW (dashed orange curve). The insets highlight a leftward shift in the Charge Neutrality Point (CNP) under illumination. The straight black arrow indicates the photogating direction. (b) Difference between the illuminated and dark transfer curves, with arrows denoting the sweep direction and order. A small hysteresis is observed between the forward and backward sweeps.

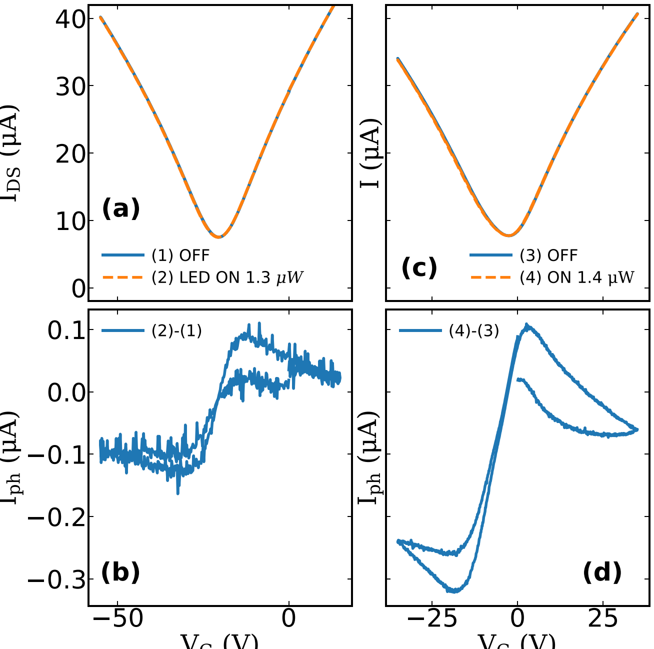

Figure 4. (a) Transfer curves for Sample 5 with and without illumination of 455 nm at 1.3 μW. (b) I_{ph} as a function of V_G. (c) Transfer curves for Sample 1 with and without illumination of 455 nm at 1.4 μW. (d) I_{ph} as a function of V_G.

4. Results

The transfer curves for Sample 2, presented in figure 3(a), compare the conditions of light OFF (blue curve) and light ON (orange dashed curve), where the sample is illuminated with 455 nm light at 1.3 μW. Upon illumination, the transfer curve shifts to the left, while maintaining the same shape, suggesting that photogating is the primary response mechanism under illumination [35, 36].

The difference between the two transfer curves in figure 3(a) is shown in figure 3(b). Subtracting the light ON curve from the light OFF curve results in negative photocurrent values for gate voltages to the left of the CNP, located between 0 and 1 V in this case, and positive values to the right of the CNP. This curve is proportional to the responsivity (see equation (1)) as a function of the gate voltage. The responsivity in the hole regime is approximately three times greater than in the electron regime. The sign of the photocurrent is negative in the hole regime and positive in the electron regime; this behavior is consistent for other samples, as seen in figure 4. A small hysteresis is observed when comparing the forward and backward sweeps, with the photocurrent being greater during the forward sweep, suggesting that the gating effect is enhanced during this part of the cycle.

The photocurrent time evolutions for Sample 2 is shown in figure 5. Figure 5(a) illustrates the current response over time for ten different wavelengths at an incident power of 1.3 μW. The data reveals a clear relationship between the wavelength of the incident light and the magnitude of the photocurrent: the amplitude increases from 850 nm (where no clear response is observed) to 365 nm (where the largest response is observed). Since there is no appreciable response at 850 nm, the data for that wavelength will be excluded from further analysis. Furthermore, from now on we focus on measurements at –15 V relative to the CNP, with additional examples of photocurrents at other operational points available in figure S2 in the SI.

Figure 5(b) illustrates how the photocurrent of Sample 2 varies over time at a wavelength of 455 nm, measured under different levels of incident power. The 10%–90% rise (or fall) times are highlighted in red for the curve with incident power of 1.74 μW, and the corresponding photocurrent is marked by the vertical red line, which is calculated using the total variation of the current in the 60 s time of illumination. As the currents have not yet reached a saturation point, this value is a lower bound for the photocurrent of the devices. Calculations for all curves were performed in the same manner. The data shows an increase in photocurrent as the incident power increases.

Absolute values of the photocurrent as a function of incident power at 455 nm follow a power-law relationship: $|I_{\mathrm{ph}}| \propto P^{\gamma}$, with $\gamma = 0.43$, as shown in figure 6. Similar results were obtained for Sample 1 with $\gamma = 0.47$ (as seen in figure S3 in the SI) and Sample 8 (300×150 μm^2) also with $\gamma = 0.47$ (figure S4 in the SI). Previous research [37] indicates that when the power-law exponent falls below 1, photogating is dominant; the smaller the exponent, the more pronounced the effect is. Thus, our data suggest a significant photogating effect in our samples. The sub-unity power dependence arises because,

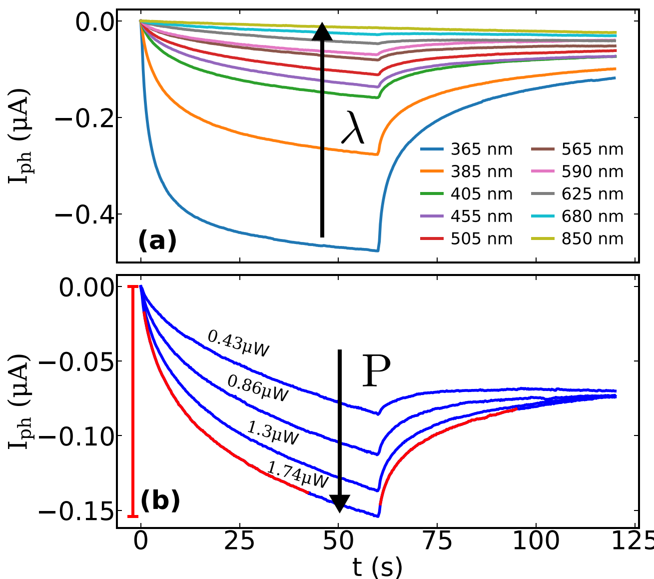

Figure 5. (a) Photocurrent generated under illumination with constant power and at various wavelengths; the power is 1.3 μW and the gate voltage is –15 V with respect to the CNP (Sample 2). (b) Photocurrent as a function of time for the same sample under 455 nm illumination for different incident powers at a gate voltage of $\Delta V_G = -15$ V from the CNP. All curves are positioned such that they have the same current of 0 A at the time the illumination starts. The 10% − 90 % rise interval for the 1.74 μW curve determining the rise time is shaded in red; for the interval from 60 to 120 s, the fall time is indicated. The rise/fall times for the other curves have been determined similarly. The magnitude of the photocurrent for 1.74 μW is represented by the vertical red line.

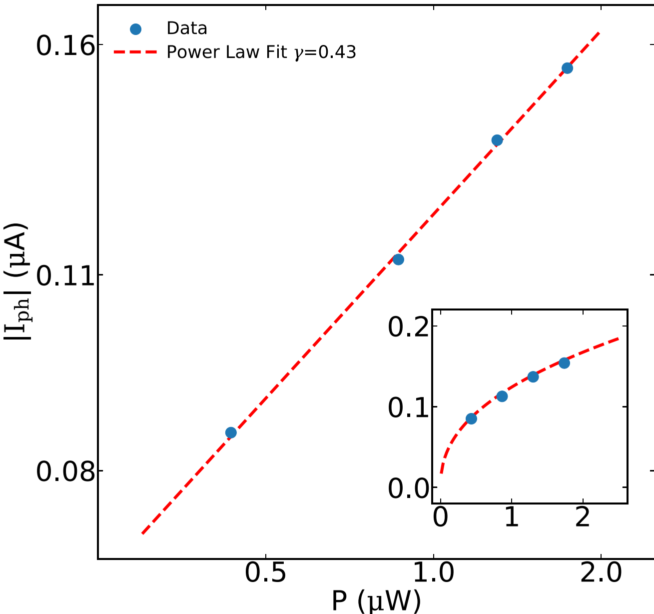

Figure 6. Absolute value of the photocurrent $|I_{ph}|$ as a function of incident power P for Sample 2 (data from figure 5). The red line represents a power-law fit, $|I_{ph}| \propto P^{\gamma}$, with $\gamma = 0.43$. The scale is log–log. The inset provides a linear representation of the same data, highlighting the sub-linear behavior as P approaches zero, which illustrates the deviation from linearity more clearly near the origin.

as the incident power increases and more photogenerated charge carriers are introduced, the trap filling becomes less efficient, leading to reduced photogating efficiency [35]. The data suggest a significant photogating effect in our samples.

Additionally, the measurements show that after the LEDs are switched off (at 60 s), the current does not return to its original value, indicating the presence of a persistent photocurrent. This is also indicative of photogating. Persistent photocurrents have been widely attributed to trapped charges, which have prolonged temporal effects, especially in the case of deep traps [38–40]. This behavior is consistently reproducible across all samples in our study (see examples in figures S5 and S6 in the SI).

The rise and fall times for samples 1 to 4, measured at $V_G = -15$ V relative to the CNP and at an incident power of 0.4 μW, are shown in figure 7 for different wavelength. The rise times, as displayed in figure 7(a), remain mostly consistent across all samples for wavelengths greater than 400 nm; however, samples with thinner Al_2O_3 layers exhibit faster rise times for shorter wavelengths. Fall times presented in figure 7(b), show that as the wavelength increases, they are less consistent between samples and the dispersion increases.

To compare the response of different configurations of SiO_2 and Al_2O_3, we illuminated samples 1, 3, 4, 6, and 7 (see table 2) with 365 nm light at an intensity of 1.4 μW. The results are presented in figure 8. The gate voltage was fixed in the hole regime: for samples 1, 3, and 4 (all with Al_2O_3), it

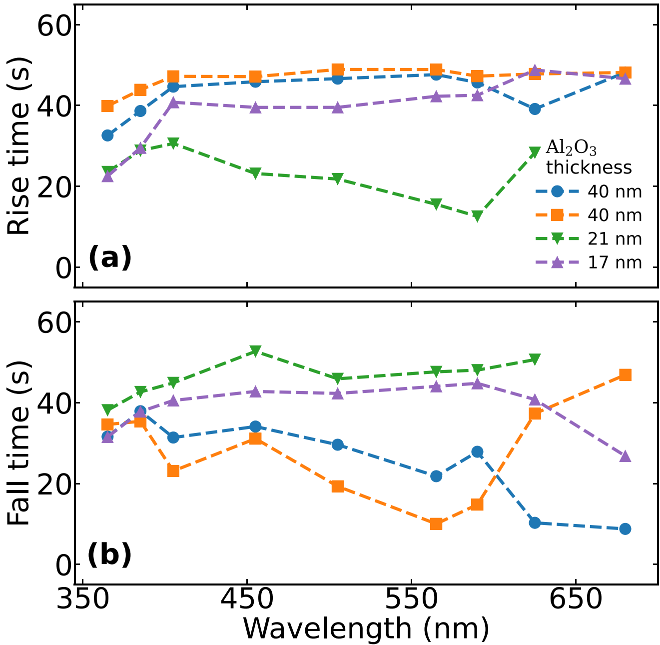

Figure 7. Rise (a) and fall (b) times for samples 1, 2, 3 and 4 (40, 40, 21 and 17 nm of Al_2O_3 respectively) as a function of wavelength. The incident power is 0.4 μW and the gate voltage with respect to the CNP is –15 V.

was set to −15 V relative to the CNP, whereas for samples 6 and 7, it was set to 13 V and 10 V, respectively, as shown in figure 9. It was observed that the thickness of the Al_2O_3 layer does not significantly affect the device response for the

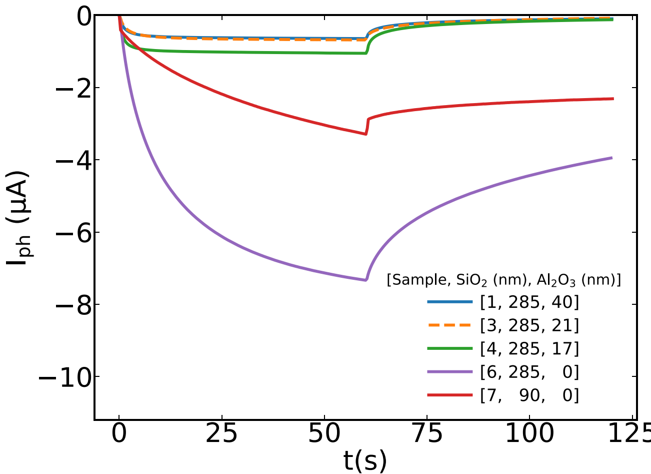

Figure 8. Response to 365 nm at 1.4 μW for samples 1, 3, 4, 6 and 7 in the hole regime. The correspondign combinations of, sample number, SiO_2 thickness and Al_2O_3 thickness are in square brackets.

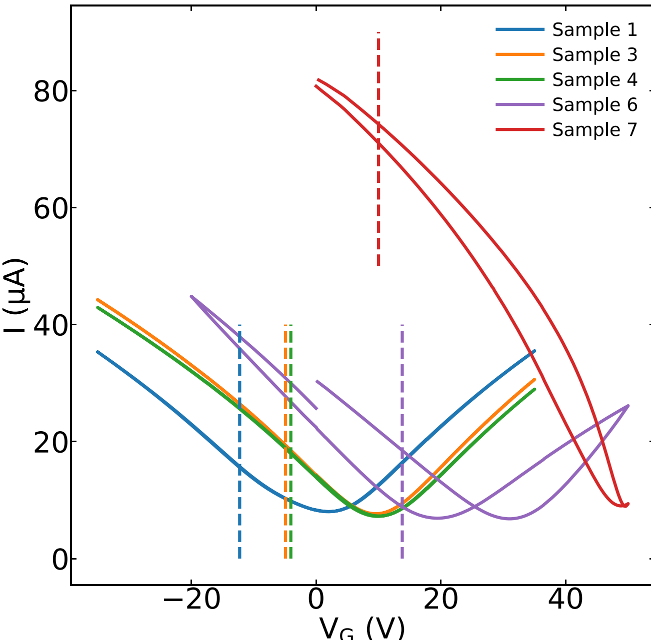

Figure 9. Transfer curves for Samples 1, 3, 4, 6, and 7 prior to the time-dependent experiments. The gate voltage set for the experiments is indicated by the corresponding colored vertical dashed lines.

devices with Al_2O_3, although it attenuates the response compared to exposed graphene. In contrast, samples with varying SiO_2 thicknesses exhibit pronounced differences in their responses, emphasizing the critical role of SiO_2 in influencing the photoresponse.

The responsivity, defined in equation (1), is presented as a function of wavelength for four different incident powers in figure 10 (Sample 2). Different colors represent different incident powers. For the longer wavelengths, the responsivity stays in the range of 0.05 A/W. As the wavelength decreases, the responsivity increases by an order of magnitude. The highest responsivity is obtained for the shortest wavelength

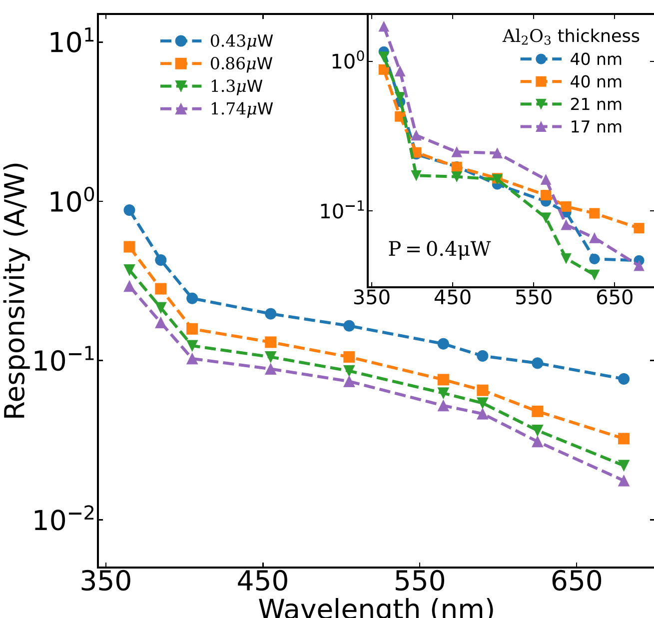

Figure 10. Responsivity of Sample 2 as a function of wavelength for four different incident powers. The gate voltage was set at −15 V with respect to the CNP point. In the inset, the responsivities for samples 1, 2, 3, and 4 are compared at an incident power of 0.4 μW and −15 V with respect to the CNP. All samples in this figure have 285 nm SiO_2.

and the lowest power, reaching 0.9 A/W. This decrease in responsivity as the incident power increases is consistent with photogating.

The inset of figure 10 illustrates the responsivities for samples 1, 2, 3, and 4 (40, 40, 21, and 17 nm Al_2O_3 respectively) as a function of wavelength for an incident power of 0.4 μW. Sample 6 (see figure7 in the SI) shows a responsivity of up to 4 A/W. However, the data for Sample 6 were taken at different gate voltages with respect to the CNP, due to the large shift of the CNP (+30 V) caused by air exposure.

Sample 9 exhibits a stable photoresponse at 455 nm, maintaining its performance over a period of 29 days, as illustrated in figures 11(a) and (b), with further stability of its transfer curve demonstrated in figure 11(c). The mobilities, labeled as μ_h^{DTM} for hole mobility and μ_e^{DTM} for electron mobility, were calculated using the direct transconductance method (DTM) [41]; more information about this can be found in the SI. These mobilities, along with the CNP, are presented in table 3, showing that Sample 9 experienced no degradation exceeding 10% over the measured time period. For comparison, the evolution of the CNP, hole, and electron mobilities for Samples 1 and 2 is also presented in table 3, and similar to Sample 9, neither of these samples exhibited degradation greater than 10% during the reported time periods. The time evolution of the transfer curves for Samples 1 and 2 is shown in figures 12(a) and (b), respectively, with Sample 2 demonstrating stable response behavior for up to 72 days. Additionally, the stability of Sample 2's time response is further illustrated in figure S8 in the SI.

The transfer curves are also stable under changes in temperature. In figure 13(a), we show the photocurrent measurements

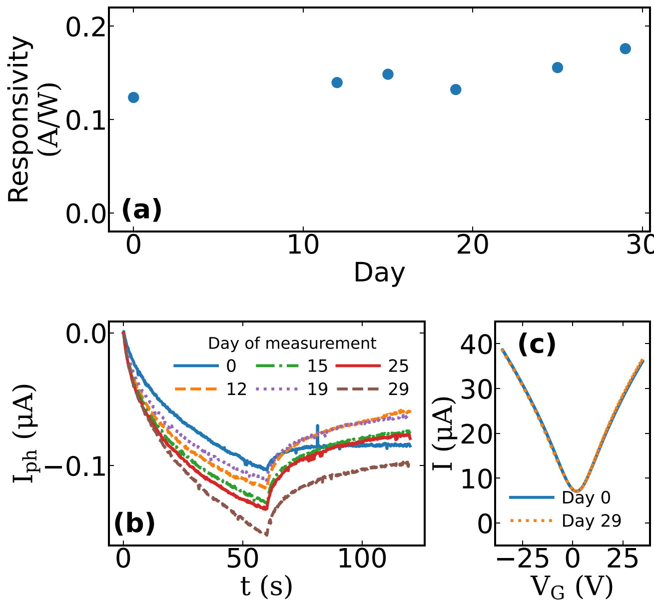

Figure 11. Stability of Sample 9, illustrated through its photoresponse at 455 nm with an incident power of 0.84 μW and an applied voltage of -15 V relative to the charge neutrality point (CNP). (a) Responsivity measured across different days. (b) Time-resolved photoresponses. (c) Transfer curves at the begining and at the end of the time interval.

Table 3. Charge Neutrality Point (CNP) voltage and carrier mobilities for Samples 1 and 2 over time.

Sample	Day	CNP (V)	μ_h^{DTM} (cm^2/V·s)	μ_e^{DTM} (cm^2/V·s)
1	0	–2.6	2449	2734
1	38	–1.8	2368	2505
2	0	0.7	2393	2619
2	72	0.6	2382	2426
9	0	1.9	2580	2620
9	29	2.1	2499	2737

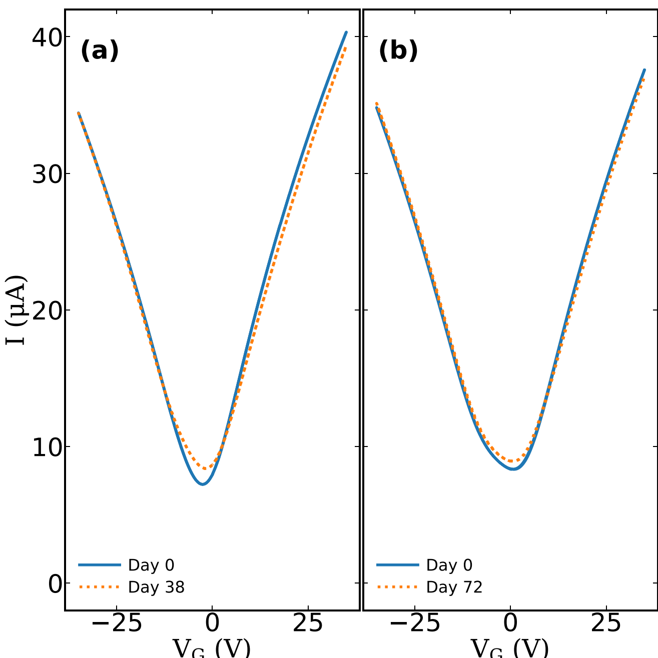

Figure 12. Transfer curves of (a) Sample 1, (b) Sample 2 with 38 and 72 days of experiments in between, respectively.

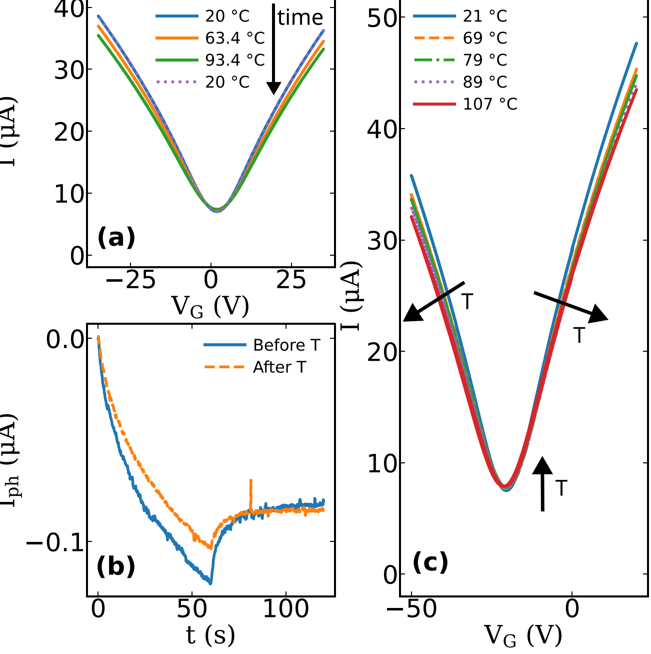

Figure 13. (a) Transfer curves as temperature changes for Sample 9. (b) Photocurrent for Sample 9 before and after being exposed to 93.4 °C. (c) Transfer curves of Sample 5 showing stability over a temperature range up to 107 °C.

for Sample 9 performed before and after increasing the sample temperature from 20 °C up to 93.4 °C and back, demonstrating a consistent response corresponding to a responsivity of $\approx$0.12 A W^{-1}. Similarly, figure 13(b) highlights the stability of the responsivity under these conditions. Lastly, figure 13(c) illustrates the temperature dependence of the transfer curves for Sample 5 at temperatures ranging from 21 °C to 107 °C. As the temperature rises, the transfer curve slightly broadens, indicating a minor decrease in charge mobility at higher temperatures. Notably, the position of the CNP remains unchanged.

5. Discussion

Many researchers have observed photogating effects in gFETs [32, 42–45]. In this scenario, excited charge carriers from the Si back gate occupy localized states at the Si/SiO_2 interface, charging the interface and altering the potential landscape over the graphene channel. This change in potential induces a horizontal shift of the CNP, of which the direction depends e.g. on the type of doping of the silicon. However, this fast interfacial response is not the only photogating process occurring in these samples, as SiO_2 can contain impurities and corresponding charge traps. The precense of long-time responses suggests that deep traps within the oxide might be involved in the process [46]. As we observe the same

photoresponse for samples without Al_2O_3 (Samples 6,7, see figure S5 in the SI), the data suggest that also in our samples the traps are located in the SiO_2. Thus, from this we conclude that although the aluminum oxide layer does not play an important role in the photogating process by charge traps, it does, however, provides reproducibility during the measurements in ambient conditions for periods of at least two months. Additionally, Al_2O_3 encapsulated samples remain stable after heating to temperatures up to 107 °C.

In all samples, we observe mainly a slow time response, associated with the filling or realasing of photogenerated charge carriers in deep traps. However, we also observe a fast response connected to interfacial photogating in Sample 7, where a thinner SiO_2 layer was used (see figures 8 and S5(f) in the SI); for the samples with the thicker SiO_2 layer the slow photogating associated with the deep traps is more apparent. Evidence suggesting that deep traps within the oxide play a crucial role in the photoresponse is presented in figure 8, where the case with a thicker SiO_2 layer exhibits a significantly greater response. The sign of the photogating is for the fast and slow processes the same: at the hole side (region left of the CNP) a negative photocurrent is observed while it is positive on the electron side. In the literature, both negative and positive signs have been reported. The opposite sign (positive photocurrent at the hole side) has also been reported for p-doped silicon substrates in [32, 42–45]. The same sign as we found was observed in [32] with a similar n-doping of the graphene under UV illumination at similar timescales. The authors attribute it to the incident light generating electron–hole pairs able to liberate adsorbates via hole recombination, which seems unlikely in our encapsulated samples.

Overall, these observations indicate that the exact mechanism of photocurrent generation depends not only on the details of the Si/SiO_2 interface (such as doping and oxide thickness) but also on other factors related to sample fabrication, such as growth conditions and the transfer process. However, a thorough investigation of these parameters is beyond the scope of the present paper, as each of them represents a research project on its own.

6. Conclusions

In our study, we present a systematic investigation of the optoelectronic performance of Al_2O_3 encapsulated CVD-grown gFETs fabricated on Si/SiO_2 wafers. We demonstrate reproducible results across samples for a wide spectrum of wavelengths, ranging from NUV to NIR. We show that the Al_2O_3 itself does not have an active role in the photogating process itself, but it increases the stability and reproducibility of samples over time while also operating in ambient conditions and at temperatures up to 107 °C. We also show that the sample performance can be tuned by changing the thickness of the SiO_2 and Al_2O_3 layer. Since the gFETs have a versatile potential in sensing applications, the durability and consistent performance of these samples over time and under changes in temperature make them ideal candidates for real-life applications in harsh conditions, e.g. radiation detection, aerospace industry [47] and operation in toxic environments under elevated temperatures.

Data availability statement

The data that support the findings of this study are available upon reasonable request from the authors.

Acknowledgments

D D acknowledges financial support from ANID Fondecyt 1220984, Fondequip EQM140055, and EQM180009, and ANILLO ATE220057. D S is supported by ANID-Subdirección de Capital Humano/Magíster Nacional/2024-22241761 master's scholarship. T P and A C G acknowledge funding from the EU FLAG-ERA Project To2Dox (JTC-2019-009) and the Spanish Ministry of Science and Innovation (Grants PID2020-115566RB-I00, TED2021-132267B-I00 and PDC2023-145920-I00).

Conflict of interest

There are no conflicts to declare.

ORCID iDs

Tomás Rojas Castiglione https://orcid.org/0000-0003-4110-8731
Thomas Pucher https://orcid.org/0009-0005-2100-8241
Guillermo Aburto Contreras https://orcid.org/0009-0006-2308-5598
Diego Sanz Biava https://orcid.org/0009-0007-9188-4495
Benjamín Briceño Elchiver https://orcid.org/0000-0002-3818-2503
Michele Buscema https://orcid.org/0009-0008-1132-0815
Andres Castellanos-Gomez https://orcid.org/0000-0002-3384-3405
Herre van der Zant https://orcid.org/0000-0002-5385-0282
Diana Dulić https://orcid.org/0000-0002-8302-5507

References

[1] Kusmartsev F, Wu W, Pierpoint M and Yung K 2015 *Appl. spectrosc. Sci. Nanomater.* **2** 191–221
[2] Bonaccorso F, Sun Z, Hasan T and Ferrari A C 2010 *Nat. Photon.* **4** 611–22
[3] Koppens F, Mueller T, Avouris P, Ferrari A, Vitiello M S and Polini M 2014 *Nat. Nanotechnol.* **9** 780–93
[4] Li J, Niu L, Zheng Z and Yan F 2014 *Adv. Mater.* **26** 5239–73
[5] Kim S, Jang M S, Brar V W, Mauser K W, Kim L and Atwater H A 2018 *Nano Lett.* **18** 971–9
[6] Xie C, Wang Y, Zhang Z-X, Wang D and Luo L-B 2018 *Nano Today* **19** 41–83
[7] Khan M A, Kumar A, Zhang J and Kumar M 2021 *J. Mater. Chem.* **9** 8129–57
[8] Anichini C and Samorì P 2021 *Small* **17** 2100514

[9] Fu J, Nie C, Sun F, Li G and Wei X 2023 *Adv. Dev. Instrum.* **4** 0031
[10] Tiwari S K, Mishra R K, Ha S K and Huczko A 2018 *Chem. Nano. Mat.* **4** 598–620
[11] Giambra M A, Mišeikis V, Pezzini S, Marconi S, Montanaro A, Fabbri F, Sorianello V, Ferrari A C, Coletti C and Romagnoli M 2021 *ACS Nano* **15** 3171–87
[12] Morales-Narváez E, Sgobbi L F, Machado S A S and Merkoçediii A 2017 *Prog. Mater. Sci.* **86** 1–24
[13] Huang W, Zhang Y, Song M, Wang B, Hou H, Hu X, Chen X and Zhai T 2022 *Chin. Chem. Lett.* **33** 2281–90
[14] Xia F, Mueller T, Lin Y-m, Valdes-Garcia A and Avouris P 2009 *Nat. Nanotechnol.* **4** 839–43
[15] Furchi M *et al* 2012 *Nano Lett.* **12** 2773–7
[16] Zhang B Y, Liu T, Meng B, Li X, Liang G, Hu X and Wang Q J 2013 *Nat. Commun.* **4** 1–11
[17] Gan X, Shiue R-J, Gao Y, Meric I, Heinz T F, Shepard K, Hone J, Assefa S and Englund D 2013 *Nat. Photon.* **7** 883–7
[18] Saeed M, Alshammari Y, Majeed S A and Al-Nasrallah E 2020 *Molecules* **25** 3856
[19] Garzón A and Villanueva Y A 2018 *J. Aerospace Technol. Manage.* **10** e4918
[20] Yavuz S, Loran E M, Sarkar N, Fenning D P and Bandaru P R 2018 *ACS Appl. Mater. Interfaces* **10** 37181–7
[21] Venkatesan B M, Estrada D, Banerjee S, Jin X, Dorgan V E, Bae M-H, Aluru N R, Pop E and Bashir R 2012 *ACS Nano* **6** 441–50
[22] Nam T *et al* 2017 *Carbon* **116** 553–61
[23] Choi D-w, Park H, Lim J H, Han T H and Park J-S 2017 *Carbon* **125** 464–71
[24] Sagade A, Neumaier D, Schall D, Otto M, Pesquera A, Centeno A, Elorza A Z and Kurz H 2015 *Nanoscale* **7** 3558–64
[25] Alexander-Webber J A *et al* 2016 *2D Mater.* **4** 011008
[26] Kim S, Nah J, Jo I, Shahrjerdi D, Colombo L, Yao Z, Tutuc E and Banerjee S K 2009 *Appl. Phys. Lett.* **94** 062107
[27] Kang C G, Lee S K, Choe S, Lee Y G, Lee C-L and Lee B H 2013 *Opt. Express* **21** 23391–400
[28] Yurgens A, Lindvall N, Sun J, Nam Y and Park Y W 2014 *JETP Lett.* **98** 704–8
[29] Nashashibi S, Koepfli S M, Schwanninger R, Baumann M, Doderer M, Bisang D, Fedoryshyn Y and Leuthold J 2024 *ACS Nano* **18** 12760–70
[30] Yang B, Zhao Y and Chen J 2021 *Nanotechnology* **32** 455503
[31] Koepfli S M *et al* 2023 *Science* **380** 1169–74
[32] Guo X *et al* 2016 *Optica* **3** 1066–70
[33] Dockx K, Barnes M D, Wehenkel D J, van Rijn R, van der Zant H S J and Buscema M 2024 *Nanotechnology* **35** 395202
[34] Quereda J, Zhao Q, Diez E, Frisenda R and Castellanos-Gomez A 2021 *Open Res. Eur.* **1** 98
[35] Fang H and Hu W 2017 *Adv. Sci.* **4** 1700323
[36] Shin J and Yoo H 2023 *Nanomaterials* **13** 882
[37] Island J O, Blanter S I, Buscema M, van der Zant H S and Castellanos-Gomez A 2015 *Nano Lett.* **15** 7853–8
[38] Bang S *et al* 2024 *Nano Lett.* **24** 9889–97
[39] Di Bartolomeo A, Genovese L, Foller T, Giubileo F, Luongo G, Croin L, Liang S-J, Ang L and Schleberger M 2017 *Nanotechnology* **28** 214002
[40] Ho P-H, Shih Y-S, Li M-K, Chen T-P, Shih F-Y, Wang W-H and Chen C-W 2018 *ACS Appl. Mater. Interfaces* **10** 38319–25
[41] Zhong H, Zhang Z, Xu H, Qiu C and Peng L-M 2015 *AIP Adv.* **5** 057136
[42] Huang Z, Liu J, Zhang T, Jin Y, Wang J, Fan S and Li Q 2021 *ACS Appl. Mater. Interfaces* **13** 22796–805
[43] Kobayashi S, Anno Y, Takei K, Arie T and Akita S 2018 *Sci. Rep.* **8** 4811
[44] Ogawa S, Shimatani M, Fukushima S, Okuda S, Kanai Y, Ono T and Matsumoto K 2019 *Opt. Eng.* **58** 057106
[45] Shimatani M, Ogawa S, Fujisawa D, Okuda S, Kanai Y, Ono T and Matsumoto K 2016 *AIP Adv.* **6** 035113
[46] Guo F, Yang B, Yuan Y, Xiao Z, Dong Q, Bi Y and Huang J 2012 *Nat. Nanotechnol.* **7** 798–802
[47] Cao F, Liu Y, Liu M, Han Z, Xu X, Fan Q and Sun B 2024 *Research* **7** 0385